Research Article Vol. 26, No. 19 | 17 Sep 2018 | OPTICS EXPRESS 24953

Optics EXPRESS

Real-time monitoring and gradient feedback enable accurate trimming of ion-implanted silicon photonic devices

BIGENG CHEN,[1,2] XINGSHI YU,[2] XIA CHEN,[2] MILAN M. MILOSEVIC,[2] DAVID J. THOMSON,[2] ALI Z. KHOKHAR,[2] SHINICHI SAITO,[3] OTTO L. MUSKENS,[1] AND GRAHAM T. REED[2,*]

[1]*School of Physics and Astronomy, Faculty of Engineering and Physical Sciences, University of Southampton, Southampton SO17 1BJ, UK*
[2]*Optoelectronics Research Centre, Faculty of Engineering and Physical Sciences, University of Southampton, Southampton SO17 1BJ, UK*
[3]*Department of Electronics and Computer Science, Faculty of Engineering and Physical Sciences, University of Southampton, Southampton SO17 1BJ, UK*
[*]*G.Reed@soton.ac.uk*

Abstract: Fabrication errors pose significant challenges on silicon photonics, promoting post-fabrication trimming technologies to ensure device performance. Conventional approaches involve multiple trimming and characterization steps, impacting overall fabrication complexity. Here we demonstrate a highly accurate trimming method combining laser annealing of germanium implanted silicon waveguide and real-time monitoring of device performance. Direct feedback of the trimming process is facilitated by a differential spectroscopic technique based on photomodulation. The resonant wavelength trimming accuracy is better than 0.15 nm for ring resonators with 20-µm radius. We also realize operating point trimming of Mach-Zehnder interferometers with germanium implanted arms. A phase shift of 1.2π is achieved by annealing a 7-µm implanted segment.

OCIS codes: (130.3120) Integrated optics devices; (250.5300) Photonic integrated circuits.

References and links

1. S. Assefa, F. Xia, and Y. A. Vlasov, "Reinventing germanium avalanche photodetector for nanophotonic on-chip optical interconnects," Nature **464**(7285), 80–84 (2010).
2. C. Sun, M. T. Wade, Y. Lee, J. S. Orcutt, L. Alloatti, M. S. Georgas, A. S. Waterman, J. M. Shainline, R. R. Avizienis, S. Lin, B. R. Moss, R. Kumar, F. Pavanello, A. H. Atabaki, H. M. Cook, A. J. Ou, J. C. Leu, Y. H. Chen, K. Asanović, R. J. Ram, M. A. Popović, and V. M. Stojanović, "Single-chip microprocessor that communicates directly using light," Nature **528**(7583), 534–538 (2015).
3. L. C. Kimerling, D. L. Kwong, and K. Wada, "Scaling computation with silicon photonics," MRS Bull. **39**(8), 687–695 (2014).
4. K. Vandoorne, P. Mechet, T. Van Vaerenbergh, M. Fiers, G. Morthier, D. Verstraeten, B. Schrauwen, J. Dambre, and P. Bienstman, "Experimental demonstration of reservoir computing on a silicon photonics chip," Nat. Commun. **5**(1), 3541 (2014).
5. M. C. Estevez, M. Alvarez, and L. M. Lechuga, "Integrated optical devices for lab-on-a-chip biosensing applications," Laser Photonics Rev. **6**(4), 463–487 (2012).
6. R. Wang, A. Vasiliev, M. Muneeb, A. Malik, S. Sprengel, G. Boehm, M. C. Amann, I. Šimonytė, A. Vizbaras, K. Vizbaras, R. Baets, and G. Roelkens, "III–V-on-Silicon Photonic Integrated Circuits for Spectroscopic Sensing in the 2–4 um Wavelength Range," Sensors (Basel) **17**(8), 1788 (2017).
7. L. T. Feng, M. Zhang, Z. Y. Zhou, M. Li, X. Xiong, L. Yu, B. S. Shi, G. P. Guo, D. X. Dai, X. F. Ren, and G. C. Guo, "On-chip coherent conversion of photonic quantum entanglement between different degrees of freedom," Nat. Commun. **7**, 11985 (2016).
8. B. Chen, H. Wu, C. Xin, D. Dai, and L. Tong, "Flexible integration of free-standing nanowires into silicon photonics," Nat. Commun. **8**(1), 20 (2017).
9. Y. Shen, N. C. Harris, S. Skirlo, M. Prabhu, T. Baehr-Jones, M. Hochberg, X. Sun, S. Zhao, H. Larochelle, D. Englund, and M. Soljacic, "Deep learning with coherent nanophotonic circuits," Nat. Photonics **11**(7), 441–446 (2017).

#334459 https://doi.org/10.1364/OE.26.024953
Journal © 2018 Received 12 Jun 2018; revised 29 Jul 2018; accepted 11 Aug 2018; published 10 Sep 2018

10. N. C. Harris, G. R. Steinbrecher, M. Prabhu, Y. Lahini, J. Mower, D. Bunandar, C. Chen, F. N. C. Wong, T. Baehr-Jones, M. Hochberg, S. Lloyd, and D. Englund, “Quantum transport simulations in a programmable nanophotonic processor,” Nat. Photonics **11**(7), 447–452 (2017).
11. B. Chen, R. Bruck, D. Traviss, A. Z. Khokhar, S. Reynolds, D. J. Thomson, G. Z. Mashanovich, G. T. Reed, and O. L. Muskens, “Hybrid Photon-Plasmon Coupling and Ultrafast Control of Nanoantennas on a Silicon Photonic Chip,” Nano Lett. **18**(1), 610–617 (2018).
12. R. Halir, P. J. Bock, P. Cheben, A. Ortega-Moñux, C. Alonso-Ramos, J. H. Schmid, J. Lapointe, D.-X. Xu, J. G. Wangüemert-Pérez, Í. Molina-Fernández, and S. Janz, “Waveguide sub-wavelength structures: a review of principles and applications,” Laser Photonics Rev. **9**(1), 25–49 (2015).
13. J. Wang, S. Paesani, Y. Ding, R. Santagati, P. Skrzypczyk, A. Salavrakos, J. Tura, R. Augusiak, L. Mančinska, D. Bacco, D. Bonneau, J. W. Silverstone, Q. Gong, A. Acín, K. Rottwitt, L. K. Oxenløwe, J. L. O’Brien, A. Laing, and M. G. Thompson, “Multidimensional quantum entanglement with large-scale integrated optics,” Science **360**(6386), 285–291 (2018).
14. W. A. Zortman, D. C. Trotter, and M. R. Watts, “Silicon photonics manufacturing,” Opt. Express **18**(23), 23598–23607 (2010).
15. P. Dong, W. Qian, H. Liang, R. Shafiiha, D. Feng, G. Li, J. E. Cunningham, A. V. Krishnamoorthy, and M. Asghari, “Thermally tunable silicon racetrack resonators with ultralow tuning power,” Opt. Express **18**(19), 20298–20304 (2010).
16. K. Padmaraju and K. Bergman, “Resolving the thermal challenges for silicon microring resonator devices,” Nanophotonics **3**(4–5), 269–281 (2014).
17. J. Schrauwen, D. Van Thourhout, and R. Baets, “Trimming of silicon ring resonator by electron beam induced compaction and strain,” Opt. Express **16**(6), 3738–3743 (2008).
18. A. Canciamilla, F. Morichetti, S. Grillanda, P. Velha, M. Sorel, V. Singh, A. Agarwal, L. C. Kimerling, and A. Melloni, “Photo-induced trimming of chalcogenide-assisted silicon waveguides,” Opt. Express **20**(14), 15807–15817 (2012).
19. A. H. Atabaki, A. A. Eftekhar, M. Askari, and A. Adibi, “Accurate post-fabrication trimming of ultra-compact resonators on silicon,” Opt. Express **21**(12), 14139–14145 (2013).
20. A. P. Knights, Z. Wang, D. Paez, and L. Dow, “Electrical trimming of the resonance of a silicon micro-ring resonator,” in *2017 IEEE 14th International Conference on Group IV Photonics (GFP)* (IEEE 2017), pp. 29–30.
21. X. Chen, M. M. Milosevic, D. J. Thomson, A. Z. Khokhar, Y. Franz, A. F. J. Runge, S. Mailis, A. C. Peacock, and G. T. Reed, “Post-fabrication phase trimming of Mach–Zehnder interferometers by laser annealing of germanium implanted waveguides,” Photon. Res. **5**(6), 578–582 (2017).
22. M. M. Milosevic, X. Chen, W. Cao, A. F. J. Runge, Y. Franz, C. G. Littlejohns, S. Mailis, A. C. Peacock, D. J. Thomson, and G. T. Reed, “Ion Implantation in Silicon for Trimming the Operating Wavelength of Ring Resonators,” IEEE J. Sel. Top. Quantum Electron. **24**(4), 8200107 (2018).
23. R. Topley, L. O’Faolain, D. J. Thomson, F. Y. Gardes, G. Z. Mashanovich, and G. T. Reed, “Planar surface implanted diffractive grating couplers in SOI,” Opt. Express **22**(1), 1077–1084 (2014).
24. R. Topley, G. Martinez-Jimenez, L. O’Faolain, N. Healy, S. Mailis, D. J. Thomson, F. Y. Gardes, A. C. Peacock, D. N. R. Payne, G. Z. Mashanovich, and G. T. Reed, “Locally Erasable Couplers for Optical Device Testing in Silicon on Insulator,” J. Lightwave Technol. **32**(12), 2248–2253 (2014).
25. T. Guo, M. Zhang, Y. Yin, and D. Dai, “A Laser-Trimming-Assist Wavelength-Alignment Technique for Silicon Microdonut Resonators,” IEEE Photonics Technol. Lett. **29**(5), 419–422 (2017).
26. D. Bachman, Z. Chen, C. Wang, R. Fedosejevs, Y. Y. Tsui, and V. Van, “Postfabrication Phase Error Correction of Silicon Photonic Circuits by Single Femtosecond Laser Pulses,” J. Lightwave Technol. **35**(4), 588–595 (2017).
27. R. Bruck, B. Mills, B. Troia, D. J. Thomson, F. Y. Gardes, Y. Hu, G. Z. Mashanovich, V. M. N. Passaro, G. T. Reed, and O. L. Muskens, “Device-level characterization of the flow of light in integrated photonic circuits using ultrafast photomodulation spectroscopy,” Nat. Photonics **9**(1), 54–60 (2015).
28. A. C. Turner-Foster, M. A. Foster, J. S. Levy, C. B. Poitras, R. Salem, A. L. Gaeta, and M. Lipson, “Ultrashort free-carrier lifetime in low-loss silicon nanowaveguides,” Opt. Express **18**(4), 3582–3591 (2010).

1. Introduction

Silicon photonics is rapidly becoming a mainstream technology with significant impact in areas such as data communication [1,2], optical information processing [3,4] and optical sensing [5,6]. It also provides a fruitful platform for fundamental research to demonstrate novel phenomena and functionalities [7–13]. To facilitate large-scale integration, tens to hundreds of photonic components are to be densely packed onto a chip at a scale of up to several cm^2 [9,10,13], hence high fabrication precision have been long pursued to improve device performance. Despite high levels of process optimization, a significant challenge remains posed by the requirement that every component completely matches the design. Fabrication errors and silicon wafer uniformity are contributing to deviations that need to be corrected after fabrication. For example, components with high quality factor are very sensitive to dimensional variations [14] which could shift the operating wavelength out of desired bandwidth due to the resulting change in effective index. Active control techniques such as integrated heaters have been developed to compensate fabrication errors by tuning the operating wavelength back to desired range [15,16]. However, the increase in system complexity and power consumption of such components is a concern as it directly impacts cost-effectiveness and power-efficiency of silicon photonics systems. Additionally, a high density of such tuning elements on a chip increases thermal loading and crosstalk, with potential loss of performance. As an alternative approach, post-fabrication trimming has been proposed and investigated as a way to realize wavelength compensation for fabrication errors on silicon photonic devices. The post-fabrication processing usually tunes operating wavelength by applying permanent alteration such as compaction, strain and additional claddings on parts or whole sections of target circuits [17–19]. Integrated heaters, fabricated in close proximity to the waveguides, were also investigated for resonant wavelength trimming by using dopant diffusion in silicon [20]. A resonant wavelength shift of 0.24 nm was achieved by applying 20 V bias for 2 hours. Recently the use of germanium (Ge) ion implantation in silicon waveguides was reported as new method for refractive index tuning which can be combined with flexible and efficient trimming ability (0.6 nm per micron of implanted length for ring resonators with 10-μm radius) [21,22]. The ion-beam implantation resulted in induced amorphization and led to large increase of refractive index, while recrystallization by annealing of the implanted segments reduced the index back close to its original value [23,24]. The implantation of Ge ions is CMOS compatible, which allows mass production. However, the trimming accuracy of post-fabrication processing methods is largely dependent on the precise knowledge of the target device status during the process. Previous studies have employed separate trimming and characterization steps [17–22,25,26]. Even when a dose for processing based on calibration results is established, other unknown variations between calibration and production devices may result in deviations. These conditions pose a challenge for accurate post-fabrication trimming using electron beam or rapid thermal annealing where real-time optical characterization of individual devices is not likely applicable.

Here we show that highly accurate trimming can be realized with laser annealing of Ge-implanted waveguide segments and real-time monitoring of device performance. As one of the most essential building blocks for silicon photonic circuits, ring resonators with implanted segments are used to demonstrate precise wavelength trimming of optical resonances. Real-time monitoring and gradient feedback is facilitated by the use of a differential spectroscopic technique, photomodulation, which not only yields the real time throughput, but also its first derivative with respect to the trimming parameter. The technique makes use of a reversible thermo-optic effect induced by the pump laser, which is used as a local perturbation to provide a dither onto the trimming process. Both broadband and narrowband spectroscopic methods were tested, the latter being more applicable to high-throughput industrial applications. Trimming accuracy better than 0.15 nm was achieved experimentally with the proposed schemes for rings with 20 μm radius, corresponding to 3% of the free-spectral range (FSR). Using photomodulation spectroscopy and 2D mapping we found that thermo-optic effect from laser heating induced a transient resonant red-shift, which can be overcome by calibration. We also performed the laser annealing on Ge-implanted Mach-Zehnder interferometers (MZIs) with real-time monitoring. 2D photomodulation maps scanned on the implanted section of an MZI before and after annealing showed that the phase difference between two arms was flipped by more than π due to the substantial change of refractive index of one arm. The developed techniques could find applications in large-scale post-fabrication trimming of silicon photonic devices with high accuracy.

2. Device fabrication and laser annealing of Ge-implanted ring resonators with real-time spectrum monitoring

Silicon photonic resonators and Mach-Zehnder interferometers were fabricated on a SOI wafer with 220 nm top silicon layer and 2 μm buried oxide layer, using electron beam lithography and inductively coupled plasma etching. A 20 nm thick silicon dioxide layer was deposited by Plasma-Enhanced Chemical Vapor Deposition (PECVD) as a protective cladding. Silicon slab thickness and the width of the rib waveguides were 100 nm and 500 nm, respectively. In the optical micrograph image [Fig. 1(a)], a segment on the right side (framed by dashed lines) of a 30-μm-radius ring resonator was partially implanted with Ge ions with energy of 130 keV and the dose of 1×10^{15} ions/cm^2, which increased the refractive index at 1550 nm from 3.46 to 3.96 according to previous studies [23]. The implanted range is denoted as the angle θ of the arc that is varied for testing. Short tapers (angle $\theta_{\text{tap}} = 5°$) with a tip width of 120 nm were formed at both ends of the implanted region which is 400 nm wide. The tapers are for suppression of reflection between the silicon part and Ge-implanted part of the waveguide, and potential resonance inside the implanted section.

In the annealing setup illustrated in Fig. 1(b), the pump light at 400 nm wavelength was generated from the second harmonics of a femto-second laser (Coherent Chameleon, pulse duration 200 fs, repetition rate 80 MHz) and was focused on the implanted segment of a ring resonator by using a microscope objective (Mitutoyo, 100X, 0.5NA). The trimming laser had an average power of 4 mW and was focused to a spot of 800 nm, resulting in an intensity of around $8\text{x}10^5$ W/cm^2 on the device. Since the pump wavelength was much smaller than the bandgap wavelength of silicon (~1.12 μm), the silicon waveguide became more absorptive, thus the heating efficiency and the trimming effect was stronger compared to a case of using an infrared laser for annealing. Standard fiber-grating couplers were employed for launching the probe as well as for collecting the output light. To characterize the shifting of the spectral resonances while trimming the device, we used a broadband spectroscopy setup. The output from an optical parametric oscillator (Chameleon Compact OPO), providing 200-fs pulses at 1550 nm with a 20 nm bandwidth, was used as the probe and the spectrum was analyzed using a grating spectrometer equipped with an InGaAs CCD array (Andor). The spectra were normalized to the spectral envelope of the probe. By scanning the microscope objective using a 3D piezo stage, the pump focus was moved along the implanted section of the ring. Figure 1(c) shows the spectra for a ring resonator with 30 μm radius as the pump was scanned along the length of the annealed segment. The resonant wavelength shift, normalized to the free-spectral range, of the mode located around 1550 nm, was extracted and plotted in Fig. 1(d) against the annealed arc length. The spectral shift shows a linear trend, with a slope of 0.09 μm^{-1} of the fitted line. Previous studies of similar devices using rapid thermal annealing in an oven [22] showed a slope of 0.17 μm^{-1}, which is almost two times larger than in our current work. This deviation is attributed to a limitation in available power of the pump laser in our current study, but the capability of tuning over more than one FSR as demonstrated here is sufficient for most applications. The measured propagation loss of ion implanted waveguides is around 30 dB/mm, which means that insertion loss of up to 0.3 dB will be added to a ring resonator if the length of an implanted segment is up to 10 μm. Experimental results revealed that the Q-factors of unimplanted and implanted ring resonators with the same radius were similar (less than 10% decrease in Q factor was observed). Therefore, an additional loss due to Ge-ion implantation would not cause substantial device performance degradation. On the other hand, annealing at high power causes a temporary spectral offset, as shown in Fig. 1(e), showing the spectra of the last annealed point and after cooling down of the ring. A blue-shift of 0.1 nm can be seen from heated status to cool status. This shift is attributed to a stationary thermo-optic effect resulting from the laser heating, which produces a red-shift to the resonance in agreement with previous studies [15,16]. Thus, high annealing powers results in some spurious thermal tuning effects that needs to be compensated in the real-time feedback response, for example using calibration.

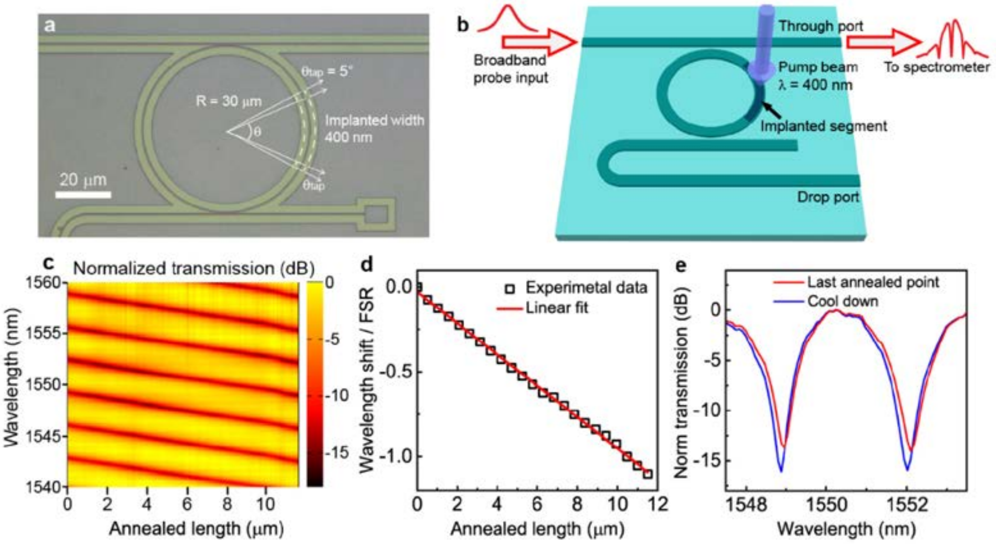

Fig. 1. Laser annealing of Ge-implanted ring resonator with real-time spectrum monitoring. (a) Optical micrograph of the ring with 30 μm radius. The dashed curves schematically indicate the implanted section on the ring. (b) Experiment setup scheme for laser annealing of implanted ring resonators with real-time spectrum monitoring. (c) Measured resonant wavelength shift of the ring as a function of annealing length. (d) Extracted resonant wavelength shift in the range from 1540 to 1560 nm normaliszed to the FSR as annealing length was varied. (d) Measurement spectrum of the last annealed point before and after cooling-down.

3. Laser annealing of Ge-implanted ring resonators with real-time gradient feedback

While the broadband spectroscopic approach discussed above provides full information over the evolution of the spectral response, industrial applications could benefit from a more simple feedback signal corresponding to the wavelength of interest. We therefore developed another real-time monitoring method for decision making on whether the trimmed wavelength has reached a target wavelength. As illustrated in Fig. 2(a), the transmission T of a probe at a single wavelength through a resonator will change with the shifting resonance during an annealing process. Ideally, if T of the through port reaches its minimum it means the resonance is located at the probe wavelength, which can be set as our target. The use of the absolute transmission T for decision making comes with a number of disadvantages. Generally, the location of the minimum can only be established once the system has already moved past it, therefore the signal strength by itself is not a good feedback indicator. Additionally, noise from the setup and from the environment, laser fluctuations, or drift in the fiber coupling will add spurious variations which complicate a precise absolute measurement of T.

Much more reliable measurements can be obtained using differential measurements to an external perturbation, which can be used to establish the relative variation ΔT normalized to T as a gradient feedback, at a well-defined modulation frequency of the perturbation. In our work we use the photomodulation response, which provides a derivative T' with respect to the tuning parameter as an indicator of the relative position of the trimmed resonance. The target position of the resonance wavelength is reached when the derivative of the resonance lineshape is zero as illustrated in Fig. 2(b). Therefore, once T' reaches zero from negative side, the resonance is aligned with the target wavelength. Taking the spatial derivative directly from the transmission signal versus anneal length would suffer from the same noise sources as the transmission itself. The photomodulation effect from the pump light in combination with lock-in amplification detection allows sensitive extraction of the feedback signal with high noise suppression. As illustrated in Fig. 2(c), an optical chopper at 80 Hz is added to the annealing pump and is synchronized with a lock-in amplifier which replaces the spectrometer from our previous setup. A narrow line tunable laser at telecom wavelength was used for the probe light. The system mainly uses the thermo-optic effect from the UV laser to obtain a periodic perturbation on the implanted waveguide's refractive index. Thus, while the annealing produces an irreversible recrystallization of the implanted region, the photomodulation response provides the reversible differential response of the system with respect to the tuning parameter, namely the local refractive index. High signal-to-noise ratio is obtained using the combination of optical chopper and lock-in detection. The photomodulation signal ΔT reflects the relative position of the probe wavelength to the resonance and can be considered as proportional to T' for a very small perturbation. This approximation still holds even with the fact that the modulation is done in one direction because the dependence of T on index perturbation Δn is linear within the tiny Δn regime. If at the same time the annealing is taking place and shifting the resonance permanently, we will see ΔT gradually changes following the curve of T' in shape. Therefore, ΔT reaching zero from a negative number indicates the target resonance wavelength has been achieved and the annealing should be stopped. Figure 2(d) gives a typical measured curve of ΔT whilst increasing the annealed length for a 20-μm-radius ring. This curve do shows a similar trend to the resonance derivative in Fig. 2(b). Again, the annealing was performed by scanning the focused pump light (average power 4 mW) on the implanted segment with an angular step as small as 0.02°. We set the probe wavelength to 1550.3 nm in order to obtain a target wavelength of 1550 nm after trial tests, which calibrated the additional thermo-optical shift effect and some delay in the feedback. The trimming laser was blocked as soon as ΔT reached zero as marked by the blue arrows in Fig. 2(d). The inset shows the corresponding T signal near $\Delta T = 0$. We note that the T signal is ambiguous around the peak between 3.5 to 4.0 μm annealed length, with fluctuations near the minimum which make the judgment very challenging. In comparison, the ΔT response shows a very precise crossing point with a precision better than 50 nm in the annealing length. The same annealing experiment using the drop port outputs yielded very similar results with opposite signs. Before and after annealing, transmission spectra of processed rings were checked with a standard high-resolution swept-frequency testing system (Agilent 8163B Lightwave Multimeter). As depicted in Fig. 2(e), a trimmed resonance is at 1549.93 nm, only 0.07 nm away from the target. The transmission spectrum before annealing is also given for comparison, revealing a 4-nm (FSR ~4.9 nm) wavelength tuning range of the laser trimming with a 7-μm annealed length. The quality factor basically remains unchanged (about 1400). In total 12 different ring resonators with 20-μm radius were trimmed for the same target wavelength 1550 nm. Figure 2(f) gives the plot of variation $d\lambda$ normalized to FSR between actual trimmed resonances and the target wavelength at 1550 nm of all the samples, among which there are 9 results (75%) within standard variation $\sigma = 3\%$ (or 0.15 nm in wavelength, as indicated by the shaded region). It is worth considering how scanning precision may affect the trimming accuracy. Based on the scanning precision of 50 nm, the trimming efficiency of 0.09 μm^{-1} and the FSR of ring resonators, a contributed error of 0.02 nm is obtained, which is an order of magnitude less than the trimming accuracy 0.15 nm. Hence, there should be other sources of error affecting the accuracy. We think that the room temperature variations during annealing and calibration could have more significant influence on the accuracy of both processing and characterization, explaining a few of the results which have larger errors.

Regarding the dynamics of the photomodulation, one would consider that the free carrier nonlinear effect might be dominant in producing periodic refractive index perturbation similar to previous studies conducted with both pulsed pump and a probe [11,27]. We have chosen a chopping speed of 80 Hz, which corresponds to a period of 12.5 ms, as it was found in experiment that this time is sufficient for heat to accumulate in a single chopping cycle to reach the annealing threshold. Thermal heating accumulates over many individual femtosecond laser pulses, and it was found that the necessary heating required for irreversible annealing took place over a time scale of hundreds of microseconds. In silicon, the free carrier lifetime is in the range of 10-100 ps [11,28]. The repetition period of our femtosecond pulses is 12.5 ns, which leaves enough time for the excited free carriers to relax before the next pulse arrives. For photomodulation experiments involving a CW probe, the reversible free carrier nonlinearity and the resultant reduction in T will be averaged over the period of the pulses by at least a factor of 125. If the free carrier effect was dominant in our photomodulation experiment, one could expect that in the case when synchronized femtosecond pulses are used as a probe, there would be over 100 times stronger $\Delta T/T$ signal, which was actually only on the similar level [11] to what we obtained in this work. On the other hand, the speed for thermal tuning of silicon resonators is in the range of 1-100 μs [15], suggesting that the thermal effect coming from each pulse can be accumulated with our dense pulse train and contribute to photomodulation. Hence, we believe that it was the thermo-optic effect that dominated in the photomodulation instead of the free carrier nonlinear effect.

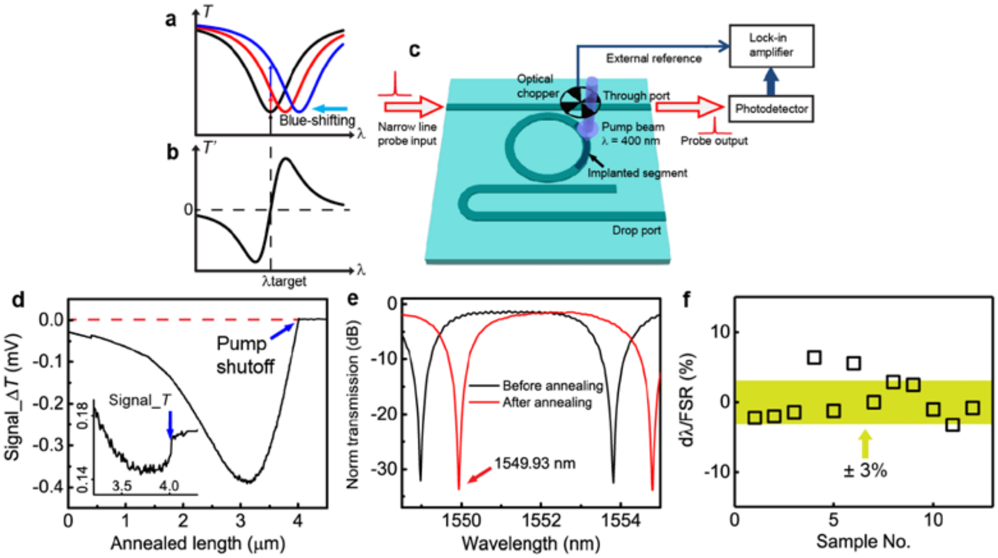

Fig. 2. Laser annealing with real-time differential transmission monitoring of Ge-implanted ring resonator. (a) Schematic spectra showing the transmission T of a ring resonance blue-shifting from blue, red to black curves. The corresponding arrows indicate the probe output change due to the shifting. (b) derivative T' of the black resonance in (a). (c) Schematic of the experimental setup used for laser annealing of implanted ring resonators with the ability of differential transmission ΔT extraction. (d) Measured signal for ΔT from a 20-μm-radius ring with annealed segment length increasing. Inset shows the corresponding T signal which shares the same labels and units of the axes with the main figure. The two blue arrows mark the $\Delta T = 0$ position at 4.01 μm. (e) Measured transmission spectra of a tested ring resonator before and after laser annealing. (f) Variation between actual trimmed resonances and target wavelength 1550 nm normalized to the FSR of all 12 samples. The obtained standard variation $\sigma = 3\%$ corresponds to 0.15 nm in wavelength.

4. Investigation of laser annealing process by 2D photomodulation mapping

To investigate in more detail the trimming process, we performed an experiment where a more detailed photomodulation mapping was done while at the same time the annealing was applied. By using a 2D scan in a raster-like pattern, we obtained simultaneous photomodulation maps of the implanted segment of a ring resonator with 20-μm radius during the laser annealing, as shown in Fig. 3. The pump beam was scanned outwards along the radial direction crossing the waveguide at a certain radial angle as indicated by the straight grey arrow in Fig. 3(a), and then the next radial scan was repeated with the angle increased by a fixed step of 0.02°. In this way we scanned the waveguide arc from 0° to 20° and covered 2 μm long in the radial direction with the waveguide located in the middle of this 2 μm wide section. Output signals T and ΔT were collected from the drop port at each annealing step simultaneously. As the scan was done at a high power for trimming (4 mW), annealing of the device was accumulated during the scan with the increasing angle while along only one radial path the annealing effect wasn't strong enough to produce big change on T with limited annealed area. Figures 3(a) and 3(b) shows the obtained photomodulation maps for T and ΔT, respectively. The condition $\Delta T = 0$ across the waveguide is framed by dashed lines in the ΔT map and emphasized by the white regions in the color map. The radial profile of this line is bent towards larger arc angle on the waveguide, corresponding to the shift of the feedback signal due to laser heating. Away from the waveguide the pump still produces a measurable ΔT response caused by thermo-optic effect but the heating effect is evidently weaker than that on the waveguide. For the same area in the map of the T signal in Fig. 3(a), a decreased output can be seen (shown in the inset) when the pump was on the waveguide, mainly because of some reversible losses induced by the pump. In more detail, what happened on the scanning line (indicated by the straight grey arrows) starting from point 1 where $\Delta T = 0$ was: after the previous annealing, ΔT was already at zero at the beginning of this radial scan; however as the pump beam approached the implanted waveguide, the thermo-optic effect red-shifted the resonance a little and raised ΔT [inset of Fig. 3(b)]. When the pump beam passed and moved away from the waveguide, the red-shift gradually disappeared and ΔT became zero again. This interpretation can also explain the bending direction as the annealing process looks slightly delayed on the waveguide and thus the process tends to overshoot the optimum thus requiring the calibration offset. The map for $\Delta T/T$ is also plotted in Fig. 3(c), which resolves another $\Delta T = 0$ area (denoted as ii) corresponding to the valley of the resonance with a similar bending feature. These results help us understanding the interplay between different optical effects induced by the pump light on the Ge-implanted circuit during laser annealing, which can in turn be used to improve the performance of this trimming process.

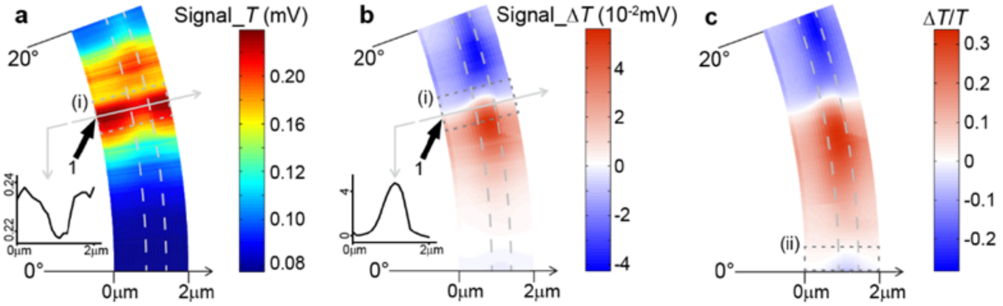

Fig. 3. Photomodulation maps of T (a), ΔT (b) and $\Delta T/T$ (c) from a Ge-implanted segment of a ring with 20-μm radius. These results were obtained from one scanning run. Inset of (a) and (b) give the profiles along the straight grey arrows across the waveguide, respectively. The units of the vertical axes are the same as that of the color bar. The curved dashed lines outline the position of the waveguide. The thin grey arrows in (a) and (b) indicate a scanning along the radial direction when the probe wavelength is near the resonance peak. Rectangle dashed Frame (i) shows the area of $\Delta T = 0$ around the resonance peak while dashed Frame (ii) shows the $\Delta T = 0$ area around the resonance valley.

5. Laser annealing of the Ge-implanted MZI with real-time monitoring

We used the same technique of gradient feedback to trim the operating point of MZIs using the setup as shown in Fig. 2(b). Figure 4(a) shows a schematic layout of the tested MZI. The inset shows an optical micrograph of the implanted arms with a different color from that of intrinsic silicon waveguides under the microscope. The longer segment is 7 μm in length, while the short segment is 2 μm long. The short segment has the purpose of balancing the loss of the two arms and is not annealed in our study. While slightly reducing the overall device throughput, the loss introduced by the short segment balances the output amplitudes of the two arms to achieve larger extinction ratio, which is important for optical modulation. Multimode interference (MMI) couplers were used for the optical splitter and combiner of the fabricated MZIs. Tapers were used for inputs and outputs of the MMIs to enhance transmission. During annealing, the pump beam was scanned along the 7-μm segment linearly to change the phase difference between the two arms, while Output 1 was coupled to the photodetector and lock-in amplifier for T and ΔT signal collection. Due to the small optical path difference between the two arms, the FSR of the MZI is much wider than the telecom range and we can use ultrafast laser pulses with relatively large (20 nm) bandwidth as the probe for optical characterization. Figures 4(b) and 4(c) depict the respective curves of T and ΔT for an annealing scan covering the whole 7-μm implanted segment plus some of the intrinsic silicon parts on both sides. The average pump power was 2.4 mW. Significant change of T started from position 0 μm and ended at 6.5 μm, which agrees well with the actual implanted length. A gradual increase of the signal is seen at the edges of the implantation area, which is attributed to the convolution with the Gaussian profile of the trimming laser and gradient in the implantation region. Taking into account this initial gradient, we estimate that the ΔT curve starts around −1.0 mV at the beginning of the section and then further decreases showing a minimum value of −1.8 mV at around 3 μm. This minimum indicates the location of the quadrature point of the MZI with the largest derivative, which is of great interest for optical modulation purpose as it can offer the highest modulation efficiency. The small discontinuity of ΔT is attributed to a step error from our slip-stick piezo stage along the line scan. It is well known that the phase-dependent transmission of an MZI output follows the trend of $(1 + \cos \varphi)$, where φ is the phase difference between the two arms. Therefore the derivative of the transmission should exhibit a trend of $-\sin \varphi$. Since ΔT is proportional to the derivative and its negative maximum ($\varphi = 0.5\pi$) is about −1.8 mV, comparing with the value of ΔT at the start of the implanted segment we can estimate that the change of phase difference $\Delta\varphi$ is about 0.72π when the whole implanted section is annealed by the pump. Larger $\Delta\varphi$ could be realized by repeating the annealing cycle several times, as is shown in Figs. 4(d) and (e). In these diagrams, both the T and ΔT signals were mapped onto the expected behaviour of the MZI using $\Delta\varphi$ as a free parameter. A maximum extinction of −15 dB was achieved at the minimum of the transmission, indicating roughly equal amplitudes in both arms of the implanted MZI as was found in earlier work [21]. Notably, the sign of the differential ΔT changes as the transmission T crosses the minimum. Ultrafast photomodulation scans showing the value of the differential transmission $\Delta T/T$ were taken on the implanted arms before and after annealing and are shown in Figs. 4(f) and 4(g), respectively. During these measurements a low pump power of 0.5 mW was used to avoid any annealing effect. The flipping of photomodulation directions for both arms can be clearly observed from the maps and the implanted segments are quite outstanding from their silicon counterparts showing a higher nonlinearity for the Ge-implanted sections compared to unimplanted silicon. Our results show that laser annealing technique with real-time monitoring holds promise on trimming MZI’s operating point.

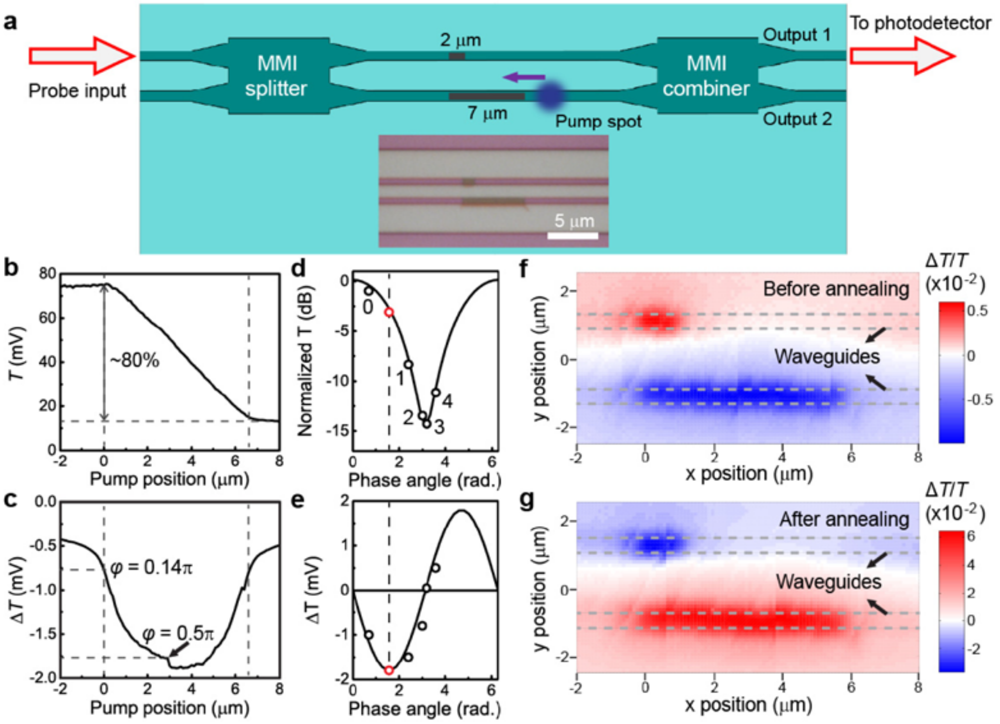

Fig. 4. Laser annealing of the Ge-implanted MZI with real-time monitoring. (a) Experiment schematic of the laser annealing with an illustrated layout of an MZI. The inset shows an optical micrograph of the two implanted arms. (b) Measured transmission (*T*) signal dependent on the pump spot position during the scanning along the whole 7-μm implanted section. (c) Corresponding measured Δ*T* signal dependent on the pump spot position. (d) and (e) Resulting values of *T* and Δ*T* for four subsequent annealing cycles, labelled 1-4 in (d), with red dot corresponding to balanced working point as determined from minimum in Δ*T* of (c). (f) and (g) Ultrafast photomodulation maps of the implanted sections on the two arms before and after laser annealing, respectively, showing sign reversal of the differential response.

6. Conclusion

In conclusion, we have developed accurate trimming techniques for Ge-ion implanted silicon photonic devices using real-time monitoring and a feedback control loop. Real-time monitoring of the resonant wavelength shift of the ring resonators was achieved using two different methods, monitoring the spectrum with a broadband short laser pulse or monitoring the derivative of resonant wavelength position with a narrowband laser taking the advantage of low-noise lock-in detection. In both methods a pump light is used for annealing the implanted waveguide and a probe light is used for device characterization. Calibration is required to remove a small wavelength shift because of the thermo-optic effect and measurement feedback delay. An accuracy better than 0.15 nm was achieved for trimming ring resonators with 20 μm radius, which could be further improved with more precise calibration and better temperature control of the silicon chip. We have applied the same phase trimming technique to MZIs and have achieved a maximum of about 0.72π change in phase difference between the two arms of an MZI by annealing a 7-μm-long implanted segment in a single scan, and up to 1.2π phase change for up to 4 subsequent annealing cycles. This technique is promising for adjusting operating point of MZI-based optical modulators. The demonstrated methods provide flexible and reliable approaches for trimming silicon photonic devices. Benefitting from the large variety of commercial positioning stages and wafer-scale post-fabrication testing setups, post-processing using laser annealing can be performed accurately, automatically and rapidly. In those occasions where active control is necessary, the methods reported in this paper may also help to reduce the power consumption required by correcting the performance of each device according to our design. We believe these techniques to be very promising and have a great potential to be further developed for industrial applications.

Funding

EPSRC (EP/L00044X/1, EP/N013247/1, EP/L021129/1).

Acknowledgments

We are grateful to the Engineering and Physical Sciences Research Council (EPSRC) for funding this work under the “Silicon Photonics for Future Systems”, “Electronic-Photonic convergence” and “CORNERSTONE” programs. G. T. Reed is a Royal Society Wolfson Merit award holder. He is grateful to the Wolfson Foundation and the Royal Society for funding of the award. D. J. Thomson acknowledges funding from the Royal Society for his University Research Fellowship. Xingshi Yu acknowledges the support from China Scholarship Council.